Applied Energy 126 (2014) 78–89

Contents lists available at ScienceDirect

Applied Energy

journal homepage: www.elsevier.com/locate/apenergy

A novel thermomechanical energy conversion cycle

Ian M. McKinley, Felix Y. Lee, Laurent Pilon *

Mechanical and Aerospace Engineering Department, Henry Samueli School of Engineering and Applied Science, University of California, Los Angeles, Los Angeles, CA 90095, USA

HIGHLIGHTS

- Demonstration of a novel cycle converting thermal and mechanical energy directly into electrical energy.
- The new cycle is adaptable to changing thermal and mechanical conditions.
- The new cycle can generate electrical power at temperatures below those of other pyroelectric power cycles.
- The new cycle can generate larger electrical power than traditional mechanical cycles using piezoelectric materials.

ARTICLE INFO

Article history:
Received 21 May 2013
Received in revised form 18 February 2014
Accepted 26 March 2014

Keywords:
Pyroelectric materials
Direct energy conversion
Waste heat harvesting
Ferroelectric materials
Olsen cycle
Thermomechanical energy

ABSTRACT

This paper presents a new power cycle for direct conversion of thermomechanical energy into electrical energy performed on pyroelectric materials. It consists sequentially of (i) an isothermal electric poling process performed under zero stress followed by (ii) a combined uniaxial compressive stress and heating process, (iii) an isothermal electric de-poling process under uniaxial stress, and finally (iv) the removal of compressive stress during a cooling process. The new cycle was demonstrated experimentally on [001]-poled PMN-28PT single crystals. The maximum power and energy densities obtained were 41 W/L and 41 J/L/cycle respectively for cold and hot source temperatures of 22 and 130 °C, electric field between 0.2 and 0.95 MV/m, and with uniaxial load of 35.56 MPa at frequency of 1 Hz. The performance and constraints on the operating conditions of the new cycle were compared with those of the Olsen cycle. The new cycle was able to generate power at temperatures below those of the Olsen cycle. In addition, the new power cycle can adapt to changing thermal and mechanical conditions.

1. Introduction

Harvesting thermal and/or mechanical energies that are typically wasted could contribute to more sustainable and efficient energy use. Waste mechanical energy is an unavoidable by-product of objects in motion and exists in the form of vibrations, shocks, or strains [1]. Sources of waste mechanical energy include fluid flow, household appliances, industrial equipment, motor vehicles, and structures such as buildings and bridges [1]. In addition, waste heat is the inevitable by-product of power, refrigeration, and heat pump cycles, according to the second law of thermodynamics [2]. In fact, many sources of waste heat, such as electricity generation and transportation systems, also waste mechanical energy.

The most widely used method to harvest mechanical energy is piezoelectric energy conversion [3]. It makes use of the piezoelectric effect to convert time-dependent mechanical deformations into electricity [1]. Other methods for direct mechanical to electrical energy conversion include electromagnet, electrostatic, and electroactive polymer generators [1]. Similarly, various methods are available to harvest waste heat. For example, Stirling engines [4] and organic Rankine cycles [5] have been used to convert low grade thermal energy into mechanical energy. Thermoelectric devices convert a steady-state temperature difference at the junction of two dissimilar metals or semiconductors into electrical energy [6]. By contrast, the Olsen cycle [7] performed on pyroelectric materials utilizes time-dependent temperature oscillations to convert thermal energy directly into electricity. Note that none of these energy conversion methods are capable of converting both thermal and mechanical energies directly into electricity.

Pyroelectric materials possess a temperature-dependent spontaneous polarization, defined as the average electric dipole moment per unit volume, in absence of an applied electric field [8]. A subclass of pyroelectric materials, known as ferroelectrics, has the ability to switch the direction and magnitude of the spontaneous polarization by reversing the applied electric field above the coercive electric field [9]. Pyroelectric materials are also piezoelectric, i.e., the electric charge at the material surface changes

* Corresponding author. Tel.: +1 (310) 206 5598; fax: +1 (310) 206 4830.
E-mail address: pilon@seas.ucla.edu (L. Pilon).

http://dx.doi.org/10.1016/j.apenergy.2014.03.069
0306-2619/

when the material is mechanically deformed. Applying a compressive stress in the poling direction decreases the electric displacement for a given temperature and electric field. The reduction in surface charge results in current in the external load.

This study aims to demonstrate the feasibility of a novel power cycle performed on pyroelectric materials to convert both thermal and mechanical energies directly into electrical energy. This new cycle was demonstrated on commercially available [0 0 1]-poled lead magnesium niobate-lead titanate $0.72PbMg_{1/3}Nb_{2/3}O_3$-$-0.28PbTiO_3$ (PMN-28PT) single crystals.

2. Background

2.1. Dielectric hysteresis loops

Fig. 1a and b show the isothermal bipolar hysteresis curves in the electric displacement D vs electric field E diagram (D–E loops) exhibited by a typical pyroelectric material at two different temperatures T_{cold} and T_{hot} under compressive stress σ equal to 0 and σ_H. The D–E loops under any compressive stress traveled in a counter-clockwise direction. The electric displacement D of a pyroelectric material at temperature T under electric field E and compressive stress σ can be expressed as [9,10]

$$D(E,T,\sigma) = \varepsilon_0\varepsilon_r(T,\sigma)E + P_s(T,\sigma) \quad (1)$$

where ε_0 is the vacuum permittivity (=8.854 × 10^{-12} F/m) and $\varepsilon_r(T,\sigma)$ is the large-field relative permittivity of the material at temperature T and under stress σ. The saturation polarization $P_s(T,\sigma)$ corresponds to the electric displacement in the linear fit of D vs E at large field extrapolated to zero electric field [11] and the slope of this linear fit is the product $\varepsilon_0\varepsilon_r(T,\sigma)$. Other important properties include (i) the remnant polarization $P_r(T,\sigma)$ corresponding to the polarization under zero applied electric field, (ii) the coercive field $E_c(T,\sigma)$ corresponding to the electric field required to reach zero electric displacement, and (iii) the Curie temperature T_{Curie} defined as the temperature at which a ferroelectric material undergoes a phase transition from ferroelectric to paraelectric. This phase transition temperature is typically defined as the temperature corresponding to the maximum of the real part of the complex dielectric constant for given frequency and applied electric field [12].

2.2. Single crystal PMN-PT

Single crystal PMN-xPT has been widely used in mechanical sensors and actuators and their piezoelectric and dielectric properties have been studied extensively [11,13–25]. PMN-xPT possesses large piezoelectric constants near the morphotropic phase boundary (MPB) separating rhombohedral and tetragonal phases [20]. This phase boundary in PMN-xPT corresponds to x ranging between 27.5 and 33 mol% [19].

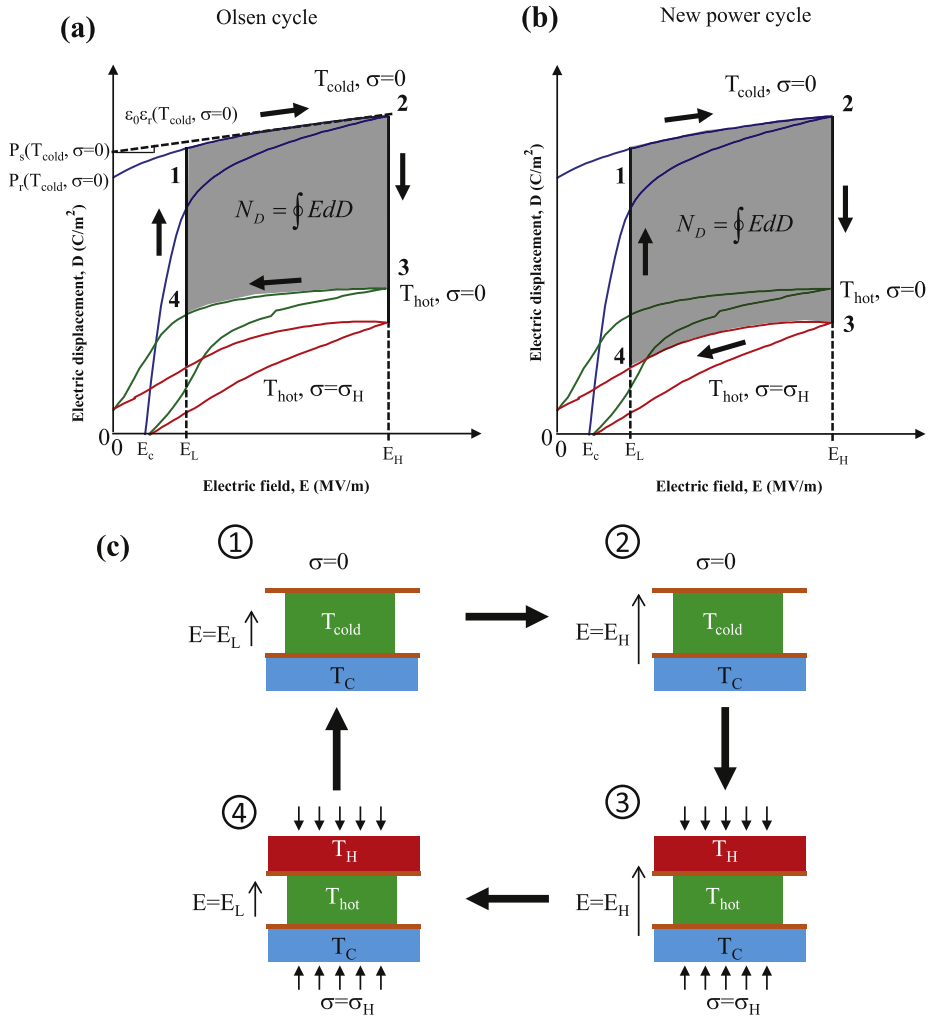

Fig. 1. Two-dimensional projections of (a) the Olsen cycle and of (b) the new power cycle in the D–E plane and electric displacement vs electric field loops at T_{cold} for uniaxial stress $\sigma = 0$ and T_{hot} for $\sigma = 0$ and σ_H. The electrical energy generated per cycle is represented by the grey areas enclosed by states 1–2–3–4. (c) The thermal, electrical, and stress states of the ferroelectric sample at each state of the new power cycle.

Properties of PMN-xPT with x between 30 and 33 mol% as functions of electric field and mechanical stress have been recently investigated[13,17]. For example, Feng et al. [13] reported the effect of uniaxial compressive stress σ, applied in the poling direction, on (i) the bipolar D–E loops at room temperature, (ii) the coercive electric field E_c, and (iii) the remnant polarization P_r for [0 0 1]-oriented PMN-30PT single crystals [13]. The remnant polarization P_r was approximately 0.25 C/m^2 under zero loading but vanished for bias compressive stress σ around 50 MPa. Similarly, Wan et al. [17] reported remnant polarizations of 0.25 and 0.30 C/m^2 at room temperature under zero load for PMN-32PT and PMN-33PT, respectively. Under compressive stress larger than 30 MPa, the remnant polarization was negligibly small ($\sim$0.08 C/m^2). Overall, the coercive field E_c and remnant polarization P_r decreased with increasing compressive stress [17,13].

Recent studies demonstrated that not only external electric field but also mechanical loading contribute to polarization switching and phase transitions in PMN-xPT single crystals [13,14,17,18]. Zhou et al. [23] compared the performance of PMN-xPT with x equal to 28%, 30%, and 32% and determined that PMN-28PT was the preferred composition for transducer, sensor, and actuator applications due to its larger piezoelectric properties in a broad temperature range. Based on these observations, single crystal PMN-28PT samples were used in the present study. The electric field vs temperature (E–T) phase diagram for [0 0 1] PMN-28PT under zero stress indicates that the material can assume four different crystalline phases in the temperature range from 27 to 177 °C for electric field between 0 and 1.5 MV/m including the monoclinic phases M_A and M_C, the tetragonal (T), and the cubic phase (C) [22]. The associated phases boundaries are both temperature and electric field dependent. At room temperature under zero electric field, the material is in the rhombohedral phase [26]. The Curie temperature at zero field was reported to be around 125 °C [22] above which a pseudocubic state existed featuring local lattice distortions [27]. An applied electric field can cause a phase transition from the pseudocubic phase to the ferroelectric state resulting in double hysteresis loops [28].

2.3. Thermomechanical cycles

Traditional thermodynamic power cycles, such as the Stirling, Rankine, and Ericsson cycles, are performed on a working fluid and convert thermal energy into mechanical work. Their efficiency is defined as the ratio of the net mechanical work produced by the cycle to the thermal energy input. These cycles are often represented in the pressure vs specific volume (p–v) diagrams. In some of them (e.g., the Rankine cycle), the working fluid undergoes liquid to vapor phase transition. Additionally, thermoelectric devices convert thermal energy to electrical energy by taking advantage of the Seebeck effect [6]. Their conversion efficiency is defined as the ratio of the electrical energy generated to the thermal energy provided at the hot junction [6]. On the other hand, in piezoelectric energy conversion, mechanical energy is converted into electrical energy. Then, the conversion efficiency is defined as the ratio of the generated electrical energy to the applied mechanical energy [29].

Alternatively, the Olsen cycle can be performed on pyroelectric materials and consists of two isothermal and two isoelectric field processes in the displacement versus electric field diagram [7]. It is analogous to the Ericsson cycle defined in the p–v diagram of a working fluid [7]. The first process of the Olsen cycle corresponds to an increase in electric field from E_L to E_H at constant temperature T_{cold}. The second process consists of heating the material from T_{cold} to T_{hot} under constant electric field E_H. The third process corresponds to a decrease in the electric field from E_H to E_L at constant temperature T_{hot}. Finally, the cycle is closed by cooling the material from T_{hot} to T_{cold} under constant electric field E_L. Note that these processes are performed under zero mechanical stress.

Fig. 1a shows the Olsen cycle in the two-dimensional D–E diagram for σ = 0 MPa. The area enclosed by the four processes previously described corresponds to the electrical energy generated per unit volume of material per cycle, denoted by N_D. It is expressed in J/L/cycle (1 J/L/cycle = 1 kJ/m^3/cycle) and defined as [7]

$$N_D = \oint EdD \tag{2}$$

The power density P_D (in W/L) is the amount of electrical energy generated by the pyroelectric material per unit volume of material per unit time. It is expressed as $P_D = N_D f$ where f is the cycle frequency.

In order to maximize the energy density N_D generated by the Olsen cycle, the electric field span ($E_H - E_L$) should be as large as possible without causing de-poling and/or electric breakdown [30]. Similarly, the electric displacement span should be the largest possible. To do so, T_{hot} should be greater than the Curie temperature T_{Curie}. Indeed, when the material is paraelectric, the spontaneous polarization vanishes. However, near T_{Curie} an applied electric field can re-pole the material. As the temperature increases above T_{Curie}, the paraelectric state becomes more and more stable and the electric field required to induce the ferroelectric state increases [22]. Thus, the cycle should be performed with T_{hot} sufficiently above T_{Curie} so that even a high electric field cannot re-pole the material.

Numerous studies have investigated the Olsen cycle performed on pyroelectric polymers [31,39–41], single crystals [32,33,42] and ceramics [7,30,34,35,36–38]. In particular, Kandilian et al. [32] studied the pyroelectric energy generation of 140 μm thick [0 0 1]-oriented PMN-32PT single crystals using the Olsen cycle. The maximum generated energy density was 100 J/L/cycle for electric field cycled between 0.2 and 0.9 MV/m and temperatures varying between 80 and 170 °C. In addition, T_{Curie} under zero field was determined to be around 150 °C [32]. Moreover, the PMN-32PT samples experienced dielectric breakdown for electric fields larger than $\sim$0.9 MV/m, and samples suffered from cracking due to thermal stress for temperature differences in excess of 90 °C [32].

The use of heat conduction to heat and cool a pyroelectric material in the Olsen cycle was explored by performing a "stamping procedure" [41]. It consisted of alternately pressing a pyroelectric sample in thermal contact with cold and hot aluminum blocks under specified electric fields. Lee et al. [41] used co-polymer 60/40 P (VDF-TrFE) films as the pyroelectric material and achieved a maximum energy density of 155 J/L/cycle at 0.066 Hz for temperatures between 25 and 110 °C electric fields between 20 and 35 MV/m. Note that single crystals and ceramics offer advantages over polymers in that (i) they possess significantly lower leakage current thanks to their higher electrical resistivity and (ii) they do not require electrical poling prior to performing the Olsen cycle. However, polymer films can sustain significantly larger electric field.

The Olsen cycle has been demonstrated to generate the largest energy densities of any power cycle performed on ferroelectric materials [43]. However, the Olsen cycle performed on a given material requires the hot source temperature to be larger than T_{Curie} in order to generate energy. Moreover, the power density of the Olsen cycle is limited by the low cycle frequency due to slow heat transfer and relaxation processes. The energy and power densities generated by a pyroelectric material undergoing the Olsen cycle could be increased by increasing the electric displacement span between temperatures T_{cold} and T_{hot}. This can be achieved by subjecting the sample to compressive stress. This is particularly true at temperatures around T_{Curie}.

Here, we present a new cycle using uniaxial compressive stress in addition to thermal and electric field cycling. It circumvents the

above mentioned difficulties to increase both energy and power densities (i) by combining piezoelectric and pyroelectric energy conversion and (ii) by increasing the cycle frequency by quickly forcing the material into a specific phase using mechanical stress instead of heating and cooling which are inherently slow. Single crystal PMN-28PT was chosen for its advantageous piezoelectric properties.

3. New thermomechanical power cycle

Fig. 1b illustrates the new power cycle projected onto the D–E plane overlaid with the corresponding isothermal bipolar hysteresis curves (D–E loops) at cold temperature T_{cold} under zero stress and at hot temperature T_{hot} under compressive stress σ_H. Fig. 1c schematically illustrates the practical implementation of the new power cycle and the stress, temperature, and electric field imposed in each state. Process 1-2 consists of an isothermal increase in electric field from E_L to E_H at T_{cold} in the absence of compressive stress. Process 2-3 corresponds to simultaneously compressing the sample at σ_H and heating it up to T_{hot}. Process 3-4 consists of an isothermal decrease in electric field from E_H to E_L at T_{hot} under compressive bias stress σ_H. Finally, process 4-1 closes the cycle by simultaneously cooling the sample to T_{cold} and removing the loading under constant electric field E_L. The area enclosed by the four processes in the D–E diagram, shown in Fig. 1b, corresponds to the generated energy density N_D defined by Eq. (2). The overall cycle frequency (in Hz) is defined as $f = (\tau_{12} + \tau_{23} + \tau_{34} + \tau_{41})^{-1}$ with τ_{ij} corresponding to the duration of process i–j. This new cycle can be implemented using a procedure similar to the "stamping procedure" [41] previously discussed but under significantly larger compressive stress. This was implemented experimentally to directly convert both thermal and mechanical energies into electrical energy using single crystal PMN-28PT.

3.1. Material efficiency

The material efficiency of a power cycle is typically defined as the ratio of the electrical energy generated by the material during the cycle to the thermal and/or mechanical energy consumed by the material to be converted by the cycle. In the present cycle, both thermal and mechanical energies are converted into electrical energy. Then, the material efficiency of the new cycle can be expressed as

$$\eta = \frac{N_D}{Q_{in} + W_{in}} \tag{3}$$

Note that this definition of efficiency is consistent with that used for piezoelectric materials given by $\eta = N_D/W_{in}$ [29] and for the Olsen cycle given by $\eta = N_D/Q_{in}$ [44]. The thermal energy provided to the material during the cycle may be expressed, per unit volume, as

$$Q_{in} = \oint \rho c_p(T) dT \tag{4}$$

where ρ and $c_p(T)$ are the density and specific heat of the ferroelectric material in kg/m^3 and J/kg K, respectively. The specific heat of ferroelectric materials $c_p(T)$ is temperature-dependent and can be measured by differential scanning calorimetry [45]. The net mechanical work W_{in} provided during the cycle per unit volume of material can be defined as

$$W_{in} = \oint \sigma(\epsilon) d\epsilon \tag{5}$$

where ϵ represents the strain in the longitudinal direction parallel to the polarization. For ferroelectric materials undergoing phase transition(s), the relationship between σ and ϵ is typically non-linear [13,46]. Thus, W_{in} cannot be expressed in terms of the Young's modulus. Instead, it should be estimated from stress–strain curves [47]. Note that the material efficiency defined above accounts for the conversion of thermomechanical energy into electricity by the material itself. It does not represent the efficiency of a potential device implementing the cycle and subject to heat losses, friction, and other irreversible processes. In other words, η represents the upper limit of a device's efficiency. The latter will also depend on the size of the system.

4. Materials and methods

4.1. Samples

Single crystal samples of PMN-28PT were purchased from Sinoceramics, LLC. The dimensions of the samples were $5 \times 5 \times 3$ mm^3. The average weight of the samples was 588.5 ± 0.8 mg, corresponding to a density of $\rho = 7847 \pm 11$ kg/m^3. These samples were poled in the [001]-direction. The two 5×5 mm^2 faces of each sample were coated with Cr/Au electrodes.

4.2. Experimental setup

The experimental setup consisted of an electrical and a thermomechanical subsystem. The electrical subsystem was a Sawyer–Tower circuit identical to that used in our previous studies [30–33,42,48]. Fig. 2a and b show a schematic and a photograph of the thermomechanical subsystem used to perform the novel power cycle, respectively. This subsystem consisted of a spring return air cylinder (McMaster–Carr 6498K252) vertically actuated using compressed air at a maximum pressure of 469 kPa. The extension and contraction of the cylinder rod were controlled by a 24 V DC solenoid valve. The heat source consisted of a 100-W cartridge heater imbedded in a 1.27 cm thick aluminum plate. A type-K thermocouple was placed at the center of the heating block. The block's temperature was kept constant using a proportional integral derivative (PID) temperature controller (Omega CN-7823). The PMN-28PT sample was sandwiched between two copper tapes to provide electrical contact between the sample's electrodes and the wires. This assembly was placed on top of a 5 mm thick steel die. An aluminum heat sink (Cool Innovations 3-151514 M) was placed in thermal contact with the steel die by epoxy adhesive OMEGABOND® 200 to passively cool the pyroelectric sample to T_{cold} during process 4-1. A 140 μm thick Kapton film was used to electrically isolate the sample's electrodes from the metallic heat source and sink. Note that the sample temperature could not be measured during electric field cycling due to electrical conduction between the sample and the thermocouple.

This setup was modified slightly when collecting isothermal D–E loops under different compressive stresses. Then, the heat sink and steel die were replaced with an aluminum heating plate and wood block identical to the heat source placed above the sample. This was done to ensure the sample was uniformly heated to T_{hot} from both sides and to minimize the temperature gradient in the sample. In this case, a type-K thermocouple placed directly on the sample was used to measure the sample temperature. It was removed before electric field cycling began.

4.3. Experimental procedure

Isothermal D–E loops under different compressive stresses were collected and the new power cycle was performed on the PMN-28PT samples using the above-described experimental setup. For comparison purposes, the Olsen cycle was also performed using

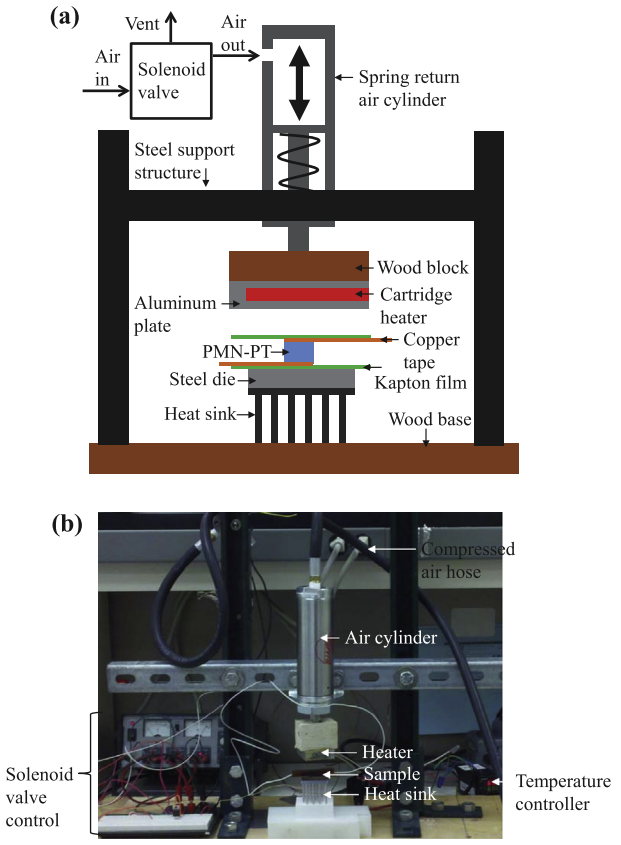

Fig. 2. (a) Schematic and (b) photograph of the thermomechanical subsystem used to create the periodic temperature oscillations and to apply compressive stress during the new thermoelectromechanical power cycle depicted in Fig. 1b. Dimensions in (a) are not to scale.

"dipping experiments" and the experimental setup described in Refs. [31,32].

4.3.1. Isothermal D–E loops

Isothermal bipolar *D–E* hysteresis loops were collected on the samples for temperature ranging between 22 and 170 °C and compressive stress varying from 0 to 25.13 MPa. These measurements were taken by applying a triangular voltage signal at 0.1 Hz across the single crystal samples. The amplitude of the applied voltage corresponded to an electric field varying from −0.75 to 0.75 MV/m. All measurements were repeated three times to assess repeatability and to estimate the experimental uncertainty.

4.3.2. Differential scanning calorimetry

Differential scanning calorimetry (DSC) measurements were performed using a Diamond DSC (by Perkin Elmer, USA). The specific heat $c_p(T)$ of the PMN-28PT sample was estimated as

$$c_p(T) = \frac{\dot{Q}_{DSC}}{m\dot{T}} \tag{6}$$

where $\dot{Q}_{DSC}$ is the measured heat transfer rate (in W) to achieve constant heating or cooling rate of $\dot{T} = dT/dt$ (in °C/s) for a sample of mass m (in kg).

The DSC instrument was successfully calibrated using an indium standard. The melting temperature at atmospheric pressure and specific phase change enthalpy were measured to be 160.8 °C and 26.9 J/g, respectively. These values fall within 2.7% and 5.6% of the properties reported in the literature [49]. The procedure to measure the specific heat c_p was also validated using an aluminum sample. The specific heat c_p of aluminum was found to be 898 J/kg K at 27 °C falling within 0.6% of the value reported in the literature [50].

4.3.3. New power cycle

The new power cycle was performed so that the duration of each process was $\tau_{23} = \tau_{41}$ and $\tau_{12} = \tau_{34} = \tau_{23}/7$. It was executed for frequency ranging from 0.025 to 1 Hz by varying τ_{23} between 17.5 and 0.438 s. The high electric field E_H varied from 0.75 to 0.95 MV/m while T_H varied from 60 to 217 °C, and the uniaxial stress σ_H applied during processes 2-3 and 3-4 ranged from 0 to 33.56 MPa. The low electric field E_L was fixed at 0.2 MV/m. The cold source temperature T_C was passively maintained near room temperature around 22 °C and never exceeded 30 °C. In addition, thermomechanical cycling was performed without electric field cycling for the above conditions on one of the samples in order to calibrate the sample temperature oscillations for different frequencies and hot source temperature T_H. To do so, a type-K thermocouple was bonded with OMEGABOND® 101 to the center of one of the 3×5 mm^2 faces.

4.3.4. Olsen cycle

The Olsen cycle was performed to achieve the maximum energy density with cold source temperature T_C set at 22 °C and hot source temperature T_H ranging from 80 to 170 °C. The electric fields E_L and E_H were fixed at 0.2 and 0.75 MV/m, respectively. The cycle frequency f was dependent on T_H based on the amount of time necessary for the sample's electric displacement to reach a minimum or maximum during the heating and cooling processes, respectively. Note that the maximum energy density for [001] PMN-28PT undergoing the Olsen cycle has previously been achieved with sample temperature $T_{cold} = 90$ °C [42]. For both cycles, the energy density generated per cycle N_D was evaluated by numerically integrating experimental data for D vs E according to Eq. (2) using the trapezoidal rule.

5. Results and discussion

5.1. Isothermal bipolar D–E loops

Fig. 3 plots the isothermal bipolar *D–E* loops measured at 0.1 Hz at temperature (a) 22 °C, (b) 80 °C, (c) 140 °C, and (d) 150 °C and under mechanical loading varying between 0 and 25.13 MPa. It illustrates the effect of compressive stress on the *D–E* loops. The isothermal *D–E* loops were closed and consecutive *D–E* loops overlapped for any temperature and compressive stress considered. This indicates that leakage current through the sample was negligibly small. The non-linearity in *D–E* loops, observed as the electric field was reduced from 0.75 to 0.0 MV/m under zero stress, corresponded to electric field induced phase transitions [28]. According to the *E–T* phase diagram at 10 Hz [22], tetragonal to monoclinic M_C phase transition occurs at 80 °C and 0.4 MV/m. Similarly, the tetragonal to cubic phase transition at temperature 140, 150, and 160 °C occurred at electric fields 0.1, 0.18, and 0.25 MV/m, respectively [22]. At $T = 170$ °C, the sample remained in the paraelectric pseudocubic phase for all electric fields considered and compressive stress had negligible effect on the *D–E* loops (not shown).

5.2. Specific heat

Fig. 4 plots the specific heat c_p of [001]-poled PMN-28PT as a function of temperature T during heating between 15 and 175 °C, followed by cooling from 175 to 15 °C. The sample mass and heating rate were $m = 148.3$ mg and $\dot{T} = 10$ °C/min, respectively. Similar results were obtained at heating rate of 5 °C/min. The measured

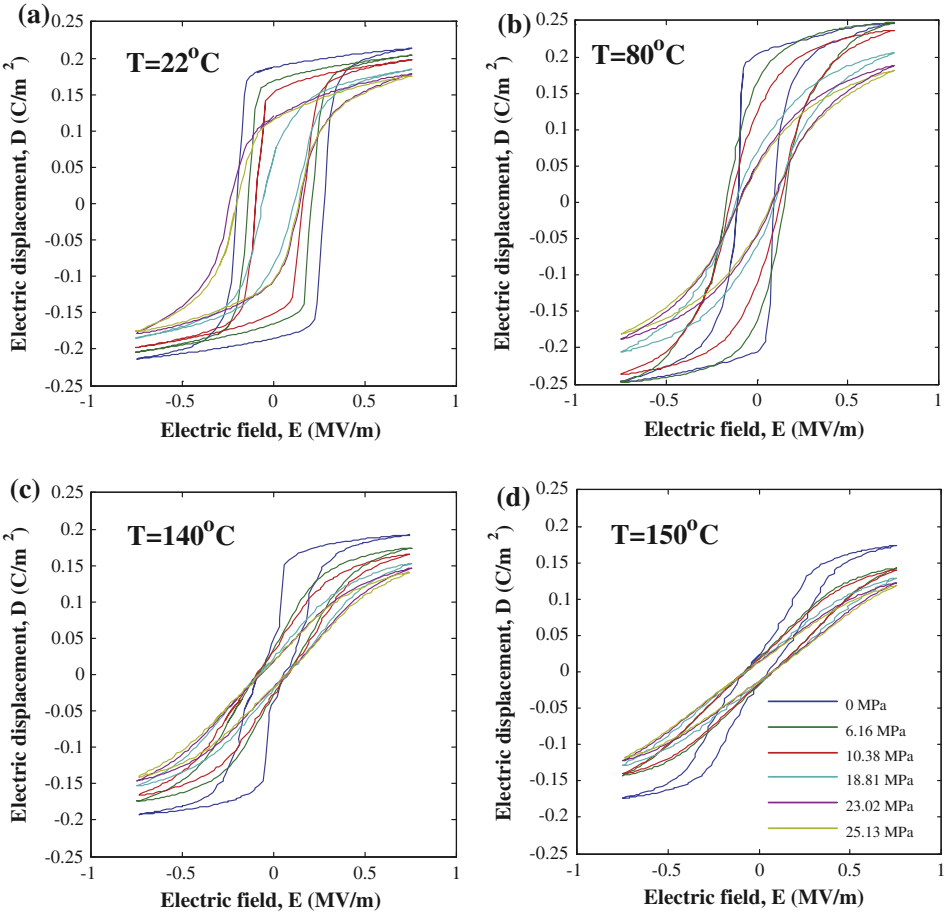

Fig. 3. Isothermal bipolar *D–E* loops of PMN-28PT Sample 1 at 0.1 Hz for temperatures (a) 22, (b) 80, (c) 140, and (d) 150 °C and compressive stress σ between 0 and 25.13 MPa.

specific heat around room temperature was in good agreement with data reported in the literature [24]. Tang et al. [24] reported the specific heat at room temperature of PMN-*x*PT single crystal to be 2.5 MJ/m^3 K over a wide range of compositions. This corresponded to 319 J/kg K assuming the density of PMN-28PT to be 7847 kg/m^3. In addition, during heating, the PMN-28PT sample exhibited peaks in c_p at the phase transition temperatures of 85 and 148 °C corresponding respectively to the monoclinic M_A to tetragonal (T) and tetragonal to cubic (C) phase transitions as suggested by the field cooling phase diagram for [001]-poled PMN-28PT [21]. During cooling, the PMN-28PT sample underwent the reverse phase transition sequence with the phase transitions occurring at 132 and 69 °C. Such thermal hysteresis [10] has also been previously observed in PMN-*x*PT compositions with *x* ranging from 0% to 25% [25].

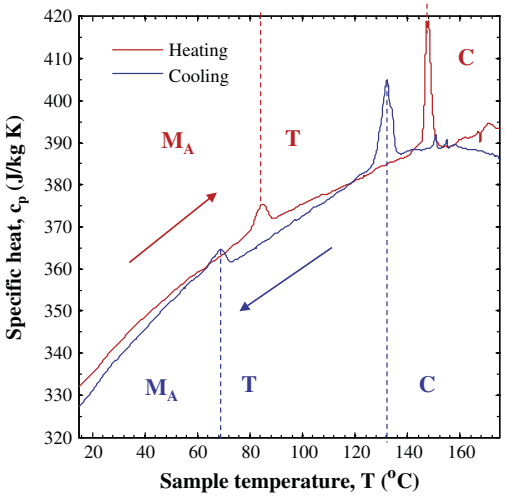

Fig. 4. Measured specific heat c_p of PMN-28PT as a function of temperature between 15 and 175 °C.

5.3. Sample temperature calibration

Fig. 5a–d show the sample temperature oscillations as a function of time for different heater temperatures T_H varying from 80 to 200 °C measured at 0.025, 0.125, 0.5, and 1 Hz, respectively. For all heater temperatures, the sample temperature took around 40 s to reach oscillatory steady-state. For a given frequency, the peak to peak temperature span and the maximum and minimum sample temperatures T_{hot} and T_{cold} increased with increasing heater temperature T_H. Fig. 6a and b show the sample temperature calibration for sample temperatures T_{hot} and T_{cold} as a function of heater temperature T_H for frequency varying from 0.025 to 1 Hz. Each data point corresponds to the arithmetic mean of T_{hot} and T_{cold} measured over five consecutive cycles in the oscillatory steady-state regime. The solid lines correspond to the linear fit of T_{hot} or T_{cold} vs T_H (in °C) for a given frequency. This fit was used to compute T_{hot} or T_{cold} for a given heater temperature and cycle frequency. In addition, the sample cold temperature T_{cold} increased

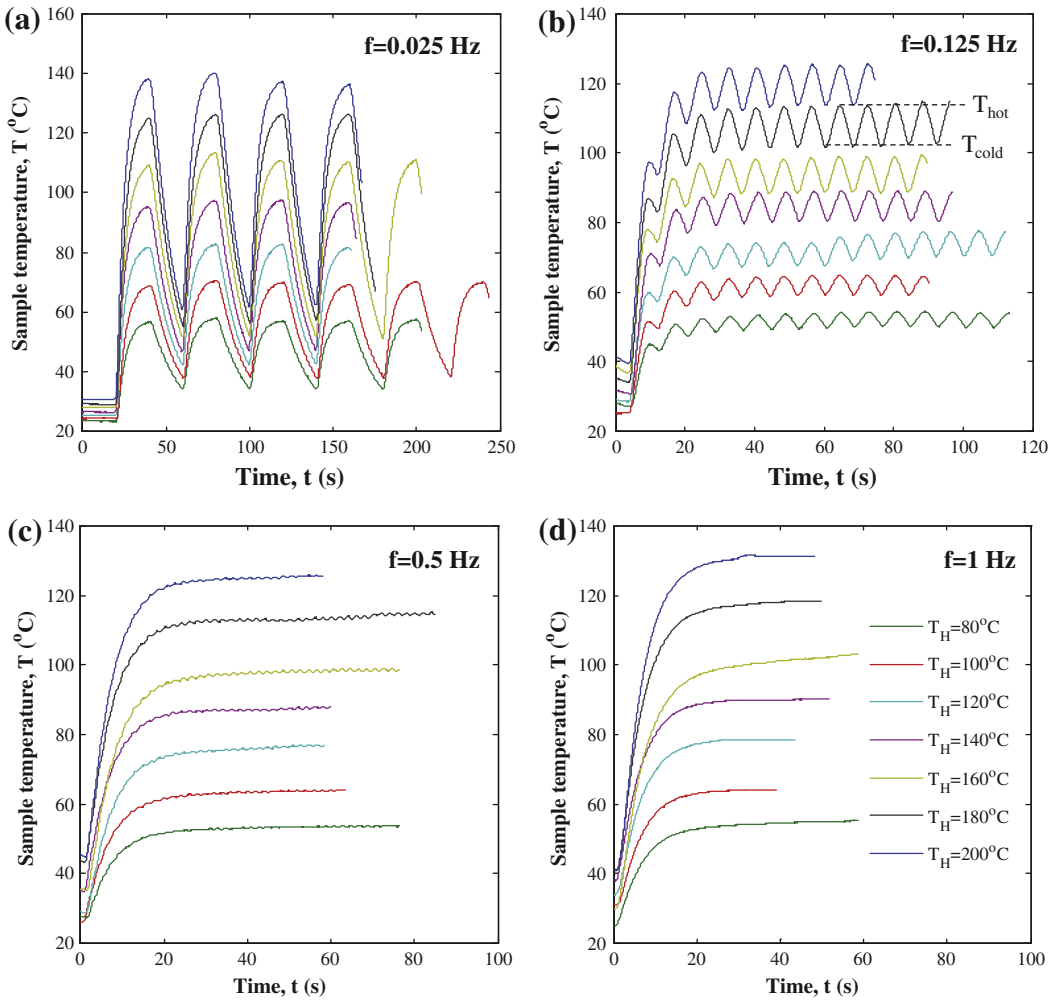

Fig. 5. (a) Sample temperature as a function of time for the new cycle performed at (a) 0.025 Hz, (b) 0.125 Hz, (c) 0.5 Hz, and (d) 1 Hz.

with increasing T_H and frequency. In fact, the difference between T_{hot} and T_{cold} decreased as the frequency increased to nearly vanish at 1 Hz. Furthermore, the sample temperature was found to be independent of compressive stress for any given heater temperature. Note that in the *D–E* loop experimental setup where the sample was heated from both top and bottom, its temperature was approximately 27 °C less than the heater temperature under steady-state conditions due to the low thermal conductivity (~0.12 W/m K) of the electrically insulating Kapton film.

5.4. Power cycle energy density comparison

Fig. 7a and b depict, in the *D–E* diagram, the new thermomechanical power cycle performed at 0.025 Hz between cold and hot source temperatures T_C = 22 °C and T_H = 157 °C or T_H = 187 °C corresponding to sample temperatures (a) T_{cold} = 52 °C and T_{hot} = 109 °C or (b) T_{cold} = 59 °C and T_{hot} = 129 °C, respectively. For both cycles, the electric field was cycled between E_L = 0.2 MV/m and E_H = 0.75 MV/m. A compressive stress of σ_H = 18.81 MPa was applied during processes 2-3 and 3-4. Based on sample temperature calibration curves (Fig. 6), the sample did not reach the cold source temperature of 22 °C, and instead, cooled to approximately 52 and 59 °C during process 4-1 before process 1-2 was performed. Fig. 7 also shows the isothermal bipolar *D–E* loops previously collected at temperatures near T_{hot} and T_{cold} and under compressive stress 0 and σ_H. The power cycles shown were vertically translated to match the electric displacement of the *D–E* loop for T_{hot} and σ_H at E_H (state 3) as performed by Olsen and Evans [51]. The new power cycles shown in Fig. 7a and b generated energy densities of 24.0 and 33.6 J/L, respectively. The Olsen cycle performed under similar operating temperatures and electric fields would yield much smaller energy densities considering the area bounded by the *D–E* loops at temperatures T_{cold} and T_{hot} [42]. In fact, it is evident from Fig. 7a that for T_{cold} = 52 °C and T_{hot} = 109 °C the Olsen cycle would generate no energy. For T_{cold} = 59 °C and T_{hot} = 129 °C, the Olsen cycle would generate approximately half of the energy density of the new cycle.

Fig. 8 plots the energy density experimentally generated (i) by the new thermomechanical power cycle at frequency 0.025 Hz and (ii) by the Olsen cycle for T_{cold} ~90 °C at frequency ranging from 0.013 to 0.021 Hz as a function of temperature T_{hot} varying between 80 and 170 °C. Note that data for the Olsen cycle corresponded to the maximum energy density [42]. Each data point represents an average over four cycles and the error bars correspond to one standard deviation or 63% confidence interval. The Olsen cycle was performed using the dipping method [31] on the same PMN-28PT sample used to perform the new cycle. The error bars associated with the Olsen cycle were larger because it was not automated, unlike the new cycle. Fig. 8 shows that, for T_{hot} between 80 and 150 °C, the energy density generated by the new power cycle was larger than that generated by the Olsen cycle. In fact, the Olsen cycle did not generate positive energy density for

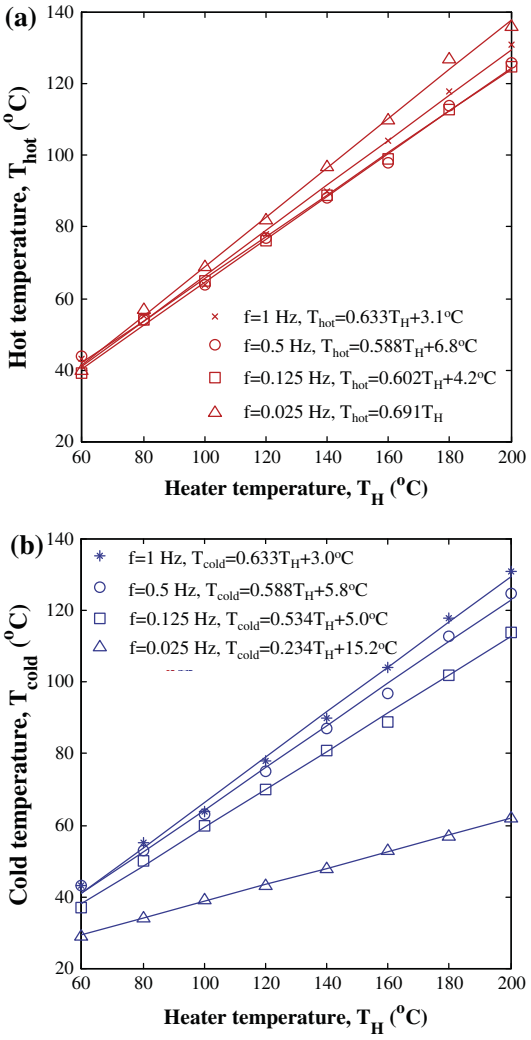

Fig. 6. Calibration curves for maximum and minimum sample temperatures (a) T_{hot} and (b) T_{cold} as functions of heater temperature T_H for frequency varying from 0.025 to 1 Hz. The lines correspond to linear fits of the experimental data for a given f.

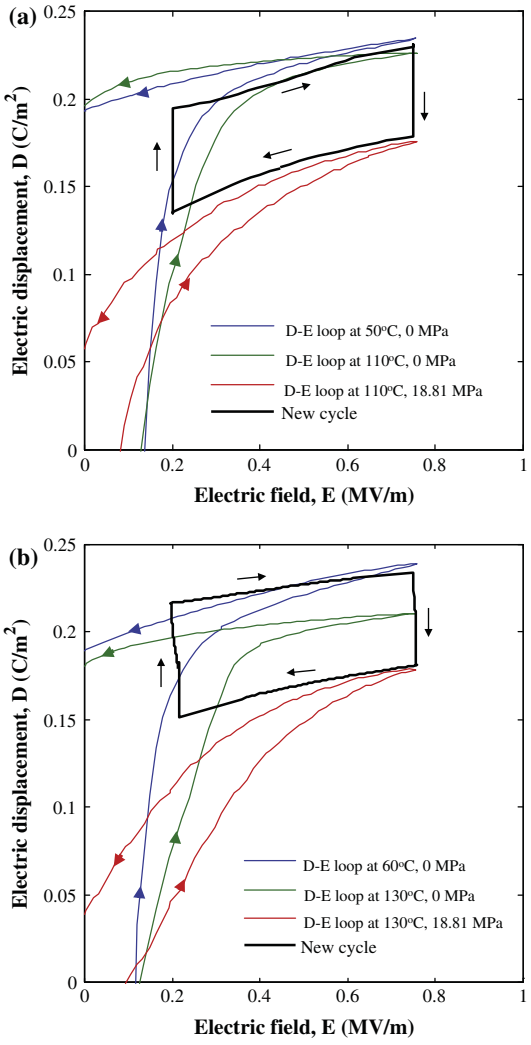

Fig. 7. Isothermal bipolar D–E loops and experimental power cycles for PMN-28PT for electric field between E_L = 0.2 MV/m and E_H = 0.75 MV/m and temperatures between (a) T_{cold} = 52 °C and T_{hot} = 109 °C or (b) T_{cold} = 59 °C and T_{hot} = 129 °C. The power cycles were performed at frequency f = 0.025 Hz. State 3 of the power cycles were vertically displaced to match the corresponding D–E loop at T_{hot} and E_H. The compressive stress applied during processes 2-3 and 3-4 was equal to 18.81 MPa.

T_{hot} below 130 °C. However, it generated the largest energy density of 85.9 J/L/cycle at $T_H = T_{hot}$ = 170 °C. Similarly, the energy density obtained with the new power cycle increased with increasing T_{hot} and reached a maximum of 42.6 J/L/cycle for T_{hot} = 150 °C.

5.5. Effect of compressive stress and temperature

Fig. 9 shows the generated energy density of the new thermo-mechanical power cycle as a function of applied compressive stress σ_H for heater temperatures T_H varying between 60 and 170 °C. Here, the frequency was fixed at 0.125 Hz while the electric field was cycled between E_L = 0.2 MV/m and E_H = 0.75 MV/m. It is evident that the energy density increased nearly linearly with increasing σ_H for any given heater temperature T_H. It also increased slightly with increasing heater temperature up to T_H = 160 °C. For this heater temperature and frequency, the sample temperature T_{cold} was 90 °C, corresponding to the temperature at which [001] PMN-28PT was in the tetragonal phase and exhibited the highest saturation polarization under zero stress [42]. On the other hand, for T_H = 170 °C and f = 0.125 Hz, T_{cold} was 96 °C, corresponding to the pseudocubic phase featuring a smaller saturation polarization than the T-phase under zero stress. Therefore, the energy density generated at 0.125 Hz for a given compressive stress was the largest for T_H = 160 °C.

5.6. Effect of frequency

Fig. 10a shows the energy density generated using the new power cycle as a function of heater temperature T_H for frequency 0.125, 0.5, and 1 Hz. The applied compressive stress σ_H was fixed at 25.13 MPa, the low and high electric fields E_L and E_H were respectively set at 0.2 and 0.75 MV/m, and the cold source temperature T_C was 22 °C. It is evident that the energy density increased with increasing heater temperature for any given frequency. In addition, it decreased only slightly with increasing cycle frequency. This was due to the fact that the change in electric displacement as a result of a change in compressive stress (process 2-3) occurred quickly and was nearly similar for all frequencies. Furthermore, longer heating and cooling durations τ_{23} and τ_{41} at lower cycle frequency allowed the slow thermal relaxation processes to take place. This enabled more charge to build up at the electrode surfaces during process 4-1 resulting in the largest N_D generated for T_H above 110 °C at 0.125 Hz. In fact, the difference between T_{cold}

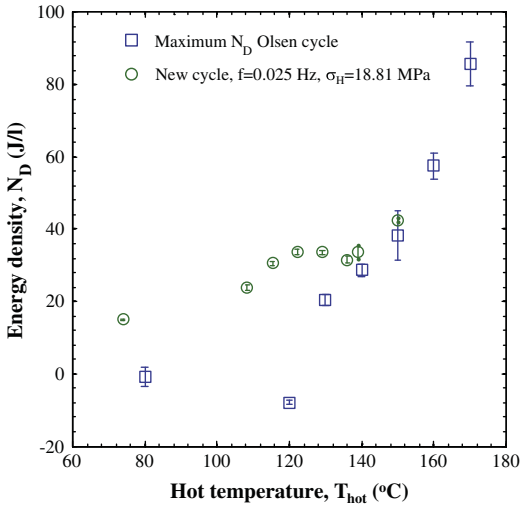

Fig. 8. Experimentally measured energy density generated with PMN-28PT as a function of hot temperature T_{hot} for maximum energy density Olsen cycles and new power cycles at 0.025 Hz. The Olsen cycle was performed with zero compressive stress (σ_H = 0 MPa) and the new power cycle was performed with σ_H = 18.81 MPa. For all cycles T_C = 22 °C, E_L = 0.2 MV/m, and E_H = 0.75 MV/m.

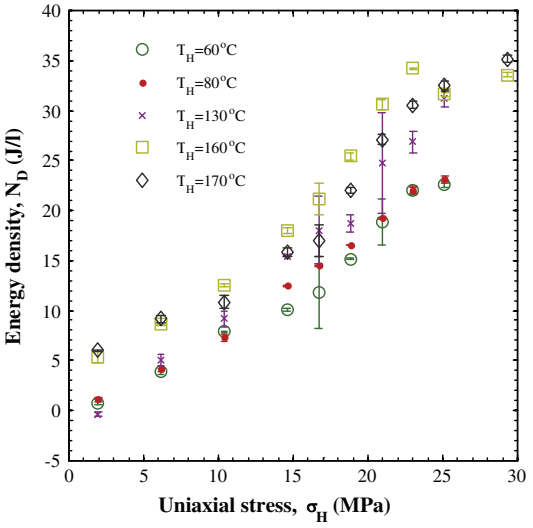

Fig. 9. Experimentally measured energy density generated by performing the new thermomechanical power cycle on PMN-28PT as a function of compressive stress. The heater temperature T_H varied from 60 to 170 °C while T_C = 22 °C, f = 0.125 Hz, E_L = 0.2 MV/m, and E_H = 0.75 MV/m.

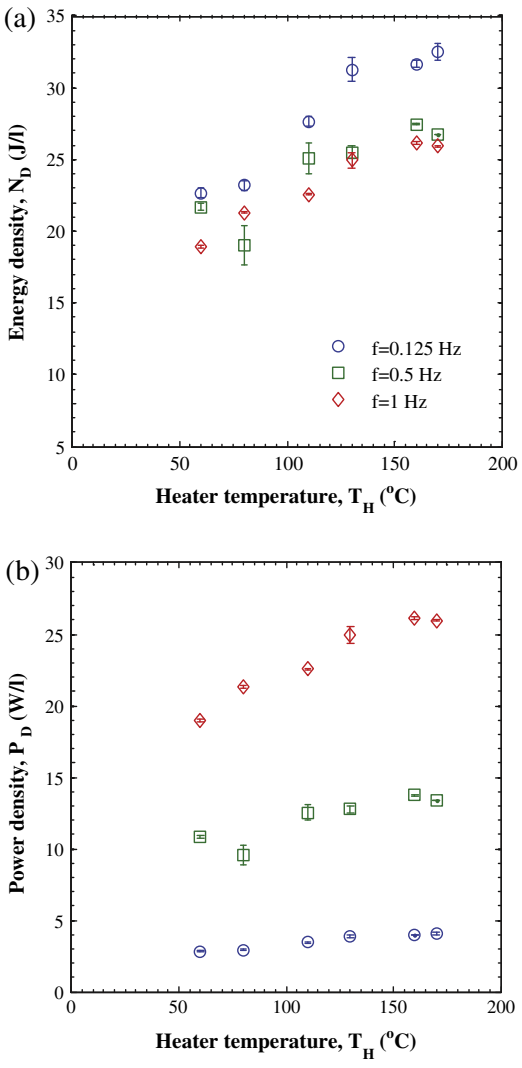

Fig. 10. Experimentally measured (a) energy density and (b) power density generated by performing the new power cycle on PMN-28PT as a function of heater temperature T_H for frequency varying from 0.125 to 1 Hz with T_C = 22 °C, E_L = 0.2 MV/m, E_H = 0.95 MV/m, and σ_H = 25.13 MPa.

and T_{hot} was around 10 °C at 0.125 Hz, while it was less than 1 °C at higher cycle frequency.

Fig. 10b shows the power density generated by the new power cycle as a function of heater temperatures T_H corresponding to the data shown in Fig. 10a. It is evident that increasing the cycle frequency resulted in significantly larger power density. In fact, the power density $P_D (= N_D f)$ at 1 Hz was nearly ten times larger than that at 0.125 Hz for heater temperature T_H above 100 °C. This can be attributed to the fact that N_D did not decrease significantly as the frequency increased from 0.125 to 1 Hz (Fig. 10a).

Fig. 11a and b show typical electric displacement changes $D–D_4$ vs time t for the new thermomechanical power cycle performed at frequency 0.125 and 1 Hz, respectively. For illustration purposes, state 4 of the cycle was used as a reference. Fig. 11a and b also show the states 1 to 4 of the cycle corresponding to those shown in Fig. 1c. In both cases, the heater temperature T_H was maintained at 160 °C, the low and high electric fields E_L and E_H were respectively 0.2 and 0.75 MV/m, and the compressive stress was σ_H = 25.13 MPa. Fig. 11a clearly illustrates the piezoelectric and pyroelectric contributions to the cycle at 0.125 Hz. During process 4-1, approximately 85% of the rise in electric displacement from 0 to 6 μC/cm^2 occurred in the first 0.25 s. This change can be attributed to the change in compressive stress from σ_H to 0 MPa. Then, the remaining 15% of the change in electric displacement during process 4-1 occurred between 0.25 and 3.5 s and can be attributed to cooling of the sample from T_{hot} = 101 °C to T_{cold} = 90 °C. In addition, Fig. 11b shows a similar response to the reduction in compressive stress during process 4-1 as the electric displacement increased from 0 to 6 μC/cm^2 in the first 0.25 s. However, at 1 Hz the sample did not have time to experience cooling during process 4-1 and no additional changes in electric displacement took place. As a result, the generated energy density as well as the overall change in electric displacement between states 4 and 2 for the cycle at 1 Hz were approximately 85% of those at 0.125 Hz. This indicates that the piezoelectric contribution to the new cycle was independent of cycle frequency between 0.125 and 1 Hz while the pyroelectric contribution decreased with increasing frequency.

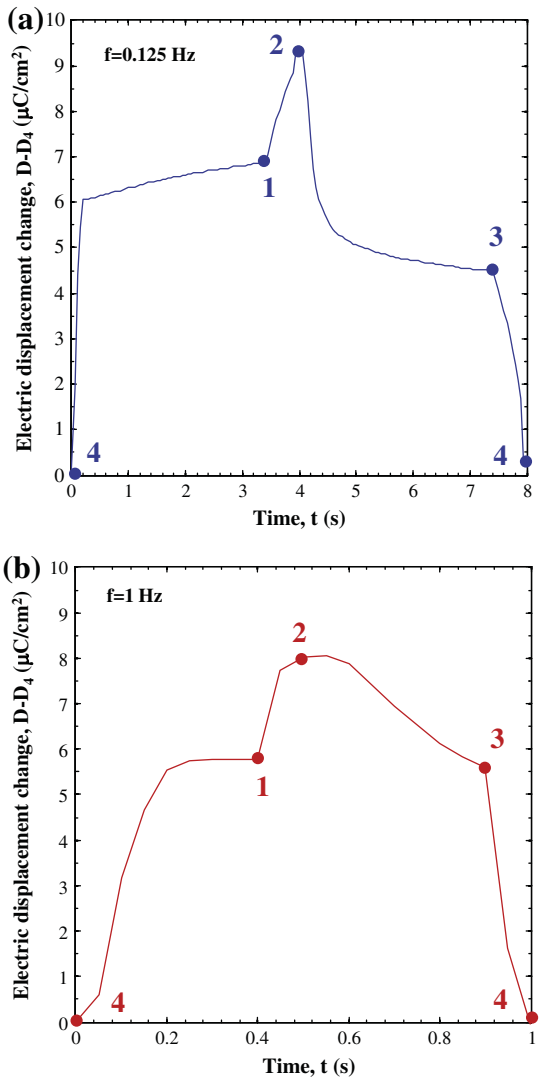

Fig. 11. Experimentally measured electric displacement vs time for the new power cycle for frequency (a) 0.125 and (b) 1 Hz. The temperature T_H was maintained at 160 °C, the low and high electric fields E_L and E_H were set at 0.2 and 0.75 MV/m, while σ_H was 25.13 MPa.

5.7. Maximum power density

Fig. 12 shows five consecutive new cycles performed on PMN-28PT in the *D–E* diagram corresponding to the maximum generated power density. The heat sink and heat source temperatures T_C and T_H were set at 22 and 130 °C, respectively. The high compressive stress σ_H was 33.56 MPa. The low and high electric fields were 0.2 and 0.95 MV/m, respectively. The cycle frequency was 1 Hz and the resulting sample temperature was $T_{hot} \simeq T_{cold} = 85$ °C, corresponding to the phase boundary between the monoclinic phase and the highly polarized tetragonal phase. The consecutive cycles nearly overlapped indicating that the cycle was highly repeatable resulting in power density of 41.3 ± 0.4 W/L.

5.8. Material efficiency

Table 1 summarizes the operating conditions, energy inputs Q_{in} and W_{in}, generated energy density N_D, and the material efficiency η obtained experimentally for various conditions of the new power cycle performed on PMN-28PT. It also gives conditions corresponding to the maximum material efficiency of the Olsen cycle. The

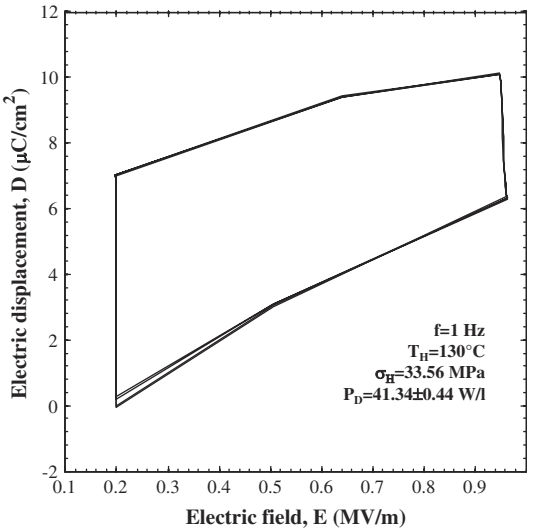

Fig. 12. *D–E* path of five consecutive cycles of the highest experimentally measured power density generated with PMN-28PT with $T_C = 22$ °C, $T_H = 130$ °C, $f = 1$ Hz, $E_L = 0.2$ MV/m, $E_H = 0.95$ MV/m, and $\sigma_H = 33.56$ MPa.

material efficiency of the thermomechanical power cycle and of the Olsen cycle was estimated using Eq. (3). The thermal energy Q_{in} was estimated according to Eq. (4) using the measured density and specific heat c_p presented in Fig. 4. The mechanical energy input W_{in} was computed from Eq. (5) using the area enclosed by the stress–strain curves at 85 °C measured at 0.2 and 0.95 MV/m for [001] PMN-28PT single crystals [52]. When the new cycle was performed at low frequency, the large heat input resulted in small efficiencies. These results illustrate the importance of operating under small temperature swings and heat input to improve the cycle efficiency.

Moreover, for a given temperature swing, the efficiency was highly dependent on the operating temperatures. For example, the two cycle performed at 0.5 Hz in Table 1 both had similar energy density N_D, the same W_{in}, and a temperature swing $T_{hot} - T_{cold} = 1$ °C, but their efficiencies differed by nearly a factor of two. This difference can be attributed to the operating temperatures. One cycle was performed between 82.3 and 83.2 °C where $c_p(T)$ exhibited a phase transition peak and a large thermal hysteresis (Fig. 4) while the other was performed between 99.9 and 100.9 °C, where no phase transition occurred. This emphasizes the importance of choosing the operating temperatures such that the heat input is minimized and the energy density is maximized in order to maximize the material efficiency η. This can be achieved by operating under adiabatic conditions at a bias temperature near the Curie temperature [52]. In fact, the maximum power density cycle performed at 1 Hz (Fig. 12) achieved an efficiency larger than 64%. In this case, the heat input was $Q_{in} = 9$ kJ/m^3 and the mechanical work performed was $W_{in} = 55$ kJ/m^3. Although the sample underwent small temperature fluctuations $T_{hot} - T_{cold} \simeq 0.1$ °C during the cycle, the corresponding thermal energy input Q_{in} was comparable to the mechanical energy W_{in}.

In addition, at low frequencies, it is important to choose T_{cold} such that heating and applying compressive stress have a similar effect on the electric displacement. The two cycles performed at 0.125 Hz in Table 1 illustrate this fact. The cycle performed between 90.4 and 103.1 °C had a material efficiency of 9.4%. In this case, the material was in the highly polarized tetragonal phase at $T_{cold} = 90.4$ °C and $E_H = 0.75$ MV/m [22]. Then, both heating and the addition of compressive stress during process 2-3 decreased the electric displacement of the material. On the other hand, for the cycle performed between 74.4 and 85.1 °C, the sample was

Table 1
List of operating conditions, energy inputs Q_{in} and W_{in}, generated energy density N_D, and material efficiency η for the new cycle and the maximum Olsen cycle efficiency. In all cases, the low electric field was $E_L = 0.2$ MV/m.

Cycle type	f (Hz)	E_H (MV/m)	T_H (°C)	T_{hot} (°C)	T_{cold} (°C)	σ_H (MPa)	W_{in} (kJ/m^3)	Q_{in} (kJ/m^3)	N_D (kJ/m^3)	η (%)
Olsen	0.021	0.75	–	170	90	0	0	540	86	15.9
TM	0.025	0.75	157	108.5	51.9	18.81	30	1202	24	2.0
TM	0.025	0.75	107	73.9	40.2	18.81	30	292	15	4.7
TM	0.125	0.75	160	103.1	90.4	25.13	41	301	32	9.4
TM	0.125	0.75	130	85.1	74.4	25.13	41	469	31	6.1
TM	0.5	0.75	160	100.9	99.9	25.13	41	21	27	43.5
TM	0.5	0.75	130	83.2	82.2	25.13	41	62	26	25.2
TM	1	0.75	160	104.4	104.3	25.13	41	2	26	60.5
TM	1	0.75	130	85.4	85.3	25.13	41	9	25	50.0
TM	1	0.95	130	85.4	85.3	33.56	55	9	41	64.1

near the phase boundary between monoclinic M_C and tetragonal at $T_{cold} = 74.4$ °C and $E_H = 0.75$ MV/m [22]. Then, during process 2-3, the electric displacement decreased with applied compressive stress and increased with heating. In this case, the material efficiency was 6.1%. Both of these cycles yielded a similar energy density, however one consumed an additional 168 kJ/m^3 of thermal energy per cycle.

Finally, note that the efficiency reported corresponds to the material's ability to convert thermomechanical energy into electricity. The efficiency of a device implementing the new cycle on PMN-28PT is expected to be significantly lower. In addition, W_{in} was estimated based on properties of PMN-28PT measured at 85 °C [52]. In practice, the mechanical work was performed at two different temperatures and the stress–strain behavior may have deviated from that at 85 °C [52]. Moreover, Q_{in} was estimated based on the specific heat $c_p(T)$ measured under zero mechanical stress. In practice, the heat input occurred under large uniaxial compressive stress known to affect the phase transition temperatures and the corresponding peaks in $c_p(T)$. Furthermore, note that the material efficiency of the Olsen cycle reached 48% of the Carnot efficiency between $T_C = 22$ °C and $T_H = 170$ °C.

6. Conclusion

This paper presented the concept and experimental implementation of a novel thermomechanical power cycle performed on [0 0 1]-poled PMN-28PT single crystals. The cycle consisted of four processes, namely (i) increasing the applied electric field under constant temperature T_{cold} and zero applied stress, (ii) simultaneously heating up to temperature T_{hot} and compressing the material under compressive stress σ_H under large electric field, (iii) decreasing the applied electric field under constant temperature T_{hot} and compressive stress σ_H, and finally (iv) simultaneously removing the applied stress and cooling the material down to T_{cold} at small electric field. Maximum energy and power densities of 41 J/L/cycle and 41 W/L were achieved with the cycle performed at 1 Hz for heat sink and heat source temperatures of 22 °C and 130 °C and electric field cycled between 0.2 and 0.95 MV/m under compressive stress 33.56 MPa. These conditions also yielded the maximum material efficiency of converting thermomechanical energy into electric energy of 64.1%. The energy density of the new cycle was found to be nearly independent of cycle frequency, while the power density and efficiency increased with increasing cycle frequency. In addition, both the energy and power densities increased with increasing compressive stress. Furthermore, the cycle was able to convert thermal and mechanical energies into electrical energy at all temperatures considered. It is also capable of maintaining constant power output for changing hot source temperature by adjusting the applied stress. Future work should consist of implementing this cycle into autonomous and integrated devices.

Acknowledgment

This research has been supported in part by NSF-IGERT program Clean Energy for Green Industry at UCLA (NSF Award 0903720). In addition, this material is based upon work supported by the NSF-IGERT Materials Training Program under Grant No. DGE-0114443.

References

[1] Despesse G, Chaillout JJ, Boisseau S, Jean-Mistral C. Energy autonomous micro and nano systems. Chapter mechanical energy harvesting. Hoboken, NJ: John Wiley & Sons Inc.; 2012.
[2] Moran MJ, Shapiro HN. Fundamentals of engineering thermodynamics. fifth ed. New York, NY: John Wiley and Sons; 2004.
[3] Anton SR, Sodano HA. A review of power harvesting using piezoelectric materials (2003–2006). Smart Mater Struct 2007;16:R1–R21.
[4] Thombare DG, Verma SK. Technological development in the Stirling cycle engines. Renew Sustain Energy Rev 2008;12:1–38.
[5] Chen H, Goswami DY, Stefanakos EK. A review of thermodynamic cycles and working fluids for the conversion of low-grade heat. Renew Sustain Energy Rev 2010;14:3059–67.
[6] Zebarjadi M, Esfarjani K, Dresselhaus MS, Ren ZF, Chen G. Perspectives on thermoelectrics: from fundamentals to device applications. Energy Environ Sci 2012;5:5147–62.
[7] Olsen RB, Bruno DA, Briscoe JM, Butler WF. A pyroelectric energy converter which employs regeneration. Ferroelectrics 1981;38:975–8.
[8] Lang SB. Sourcebook of pyroelectricity. New York, NY: Gordon and Breach, Science Publishers, Inc.; 1974.
[9] Lang SB, Das-Gupta DK. Handbook of advanced electronic and photonic materials and devices, 4. San Diego, CA: Academic Press; 2001.
[10] Lines ME, Glass AM. Principles and applications of ferroelectrics and related materials. Oxford, UK: Clarendon Press; 1977.
[11] Li Z, Xi Z, Xu Z, Yao X. Dielectric/ferroelectric response and phase transition of PMN-0.32PT single crystal. J Mater Sci Lett 2002;21:1325–7.
[12] Hooker MW. "Properties of PZT-based piezoelectric ceramics between −150 and 250 °C". In: Tech Rep NASA contractor report 1998-208708, National Aeronautics and Space Administration, Hampton, VA; 1998.
[13] Feng Z, Lin D, Luo H, Li S, Fang D. Effect of uniaxial stress on the electromechanical response of ⟨0 0 1⟩-oriented $Pb(Mg_{1/3}Nb_{2/3})O_3$–$PbTiO_3$ crystals. J Appl Phys 2005;97:024103.
[14] McLaughlin EA, Liu T, Lynch CS. Relaxor ferroelectric PMN-32PT crystals under stress and electric field loading: I-32 mode measurements. Acta Mater 2004;52:3849–57.
[15] Viehland D, Powers J. Electromechanical coupling coefficient of ⟨0 0 1⟩-oriented of $Pb(Mg_{1/3}Nb_{2/3})O_3$–$PbTiO_3$ crystals: Stress and temperature independence. Appl Phys Lett 2001;78:3112–4.
[16] Viehland D, Li J, McLaughlin EA, Powers J, Janus R, Robinson H. Effect of uniaxial stress on the large-signal electromechanical properties of electrostrictive and piezoelectric lead magnesium niobate lead titanate ceramics. Appl Phys Lett 2004;95:1969–72.
[17] Wan Q, Chen C, Shen YP. Effects of stress and electric field on the electromechanical properties of $Pb(Mg_{1/3}Nb_{2/3})O_3$–$0.32PbTiO_3$ single crystals. J Appl Phys 2005;97:024103.
[18] McLaughlin EA, Liu T, Lynch CS. Relaxor ferroelectric PMN-32PT crystals under stress, electric field and temperature loading: II-33-mode measurements. Acta Mater 2005;53(14):4001–8.
[19] Ye Z-G, Dong M. Morphotropic domain structures and phase transitions in relaxor-based piezo-/ferroelectric $(1-x)PbMg_{1/3}Nb_{2/3}O_3$–$xPbTiO_3$ single crystals. J Appl Phys 2000;87(5):2312.
[20] Park SE, Shrout TR. Ultrahigh strain and piezoelectric behavior in relaxor based ferroelectric single crystals. J Appl Phys 1997;82(4):1804.
[21] Kamzina LS, Luo H. Influence of the electric field on structural transformations and phase boundary for $PMg_{1/3}Nb_{2/3}O_3$-$xPBTiO_3$ single crystals. Phys Solid State 2009;51(11):2316–23.

[22] Herklotz A, Plumhof JD, Rastelli A, Schmidt OG, Schultz L, Dorr K. Electrical characterization of PMN-28%PT(001) crystals used as thin-film substrates. J Appl Phys 2010;108:094101.
[23] Zhou D, Wang F, Luo L, Chen J, Ge W, Zhao X, et al. Characterization of complete electromechanical constants of rhombohedral $0.72Pb(Mg_{1/3}Nb_{2/3})-0.28PbTiO_3$ single crystals. J Phys D: Appl Phys 2008;41:185402.
[24] Tang Y, Luo H. Inverstigation of the electrical properties of $(1-x)Pb(Mg_{1/2}Nb_{2/3})O_3-xPbTiO_3$ single crystals with special reference to pyroelectric detection. J Phys D: Appl Phys 2009;42:075406.
[25] Colla EV, Yushin NK, Viehland D. Dielectric properties of $(PMN)_{1-x}(PT)_x$. J Appl Phys 1998;83(6):3298–304.
[26] Guo Y, Luo H, Ling D, Xu H, He T, Yin Z. The phase transistion sequence and the location of the morphotropic phase boundary region in $(1-x)Pb(Mg_{1/3}Nb_{2/3})O_3-xPbTiO_3$ single crystal. J Phys: Condens Matter 2003;15:L77–82.
[27] Han J, Cao W. Electric field effects on the phase transitions in [001]-oriented $(1-x)Pb(Mg_{1/3}Nb_{2/3})O_3-xPbTiO_3$ single crystals with compositions near the morphotropic phase boundary. Phys Rev B 2003;68:134102.
[28] Merz WJ. Double hysteresis loop of $BaTiO_3$ at the Curie point. Phys Rev 1953;91:513–7.
[29] Chang C, Tran VH, Wang J, Fuh Y-K, Lin L. Direct-write piezoelectric polymeric nanogenerator with high energy conversion efficiency. Nano Lett 2010;10:726–31.
[30] Lee FY, Goljahi S, McKinley IM, Lynch CS, Pilon L. Pyroelectric waste heat energy harvesting using relaxor ferroelectric 8/65/35 PLZT and the Olsen cycle. Smart Mater Struct 2012;21:025021.
[31] Navid A, Pilon L. Pyroelectric energy harvesting using Olsen cycle in purified and porous poly(vinylidene fluoride-trifuoroethylene) [P(VDF-TrFE)] thin films. Smart Mater Struct 2011;20:025012.
[32] Kandilian R, Navid A, Pilon L. Pyroelectric energy harvesting capabilities of PMN-PT near the morphotropic phase boundary. Smart Mater Struct 2001;20(5):055020.
[33] McKinley IM, Kandilian R, Pilon L. Waste heat energy harvesting using the Olsen cycle on $0.945Pb(Zn_{1/3}Nb_{2/3})O_3$-$0.055PbTiO_3$ single crystals. Smart Mater Struct 2012;21(3):035015.
[34] Ravindran SKT, Huesgen T, Kroener M, Woias P. A self-sustaining micro thermomechanic-pyroelectric generator. Appl Phys Lett 2011;99(10):104102.
[35] Hunter SR, Lavrik NV, Bannuru T, Mostafa S, Rajic S, Datskos PG. "Development of MEMS based pyroelectric thermal energy harvesters". In: Proceedings of the SPIE, energy harvesting and storage: materials, devices, and applications II, Orlando, Florida, USA, April 25; 2011, vol. 8035, p. 80350V.
[36] Olsen RB. Ferroelectric conversion of heat to electrical energy – a demonstration. J Energy 1982;6:91–5.
[37] Olsen RB, Brown DD. High efficiency direct conversion of heat to electrical energy – related pyroelectric measurements. Ferroelectrics 1982;40:17–27.
[38] Olsen RB, Bruno DA, Briscoe JM. Cascaded pyroelectric energy converter. Ferroelectrics 1984;59:205–19.
[39] Olsen RB, Bruno DA, Briscoe JM. Pyroelectric conversion cycle of vinylidene fluoride-trifluoroethylene copolymer. J Appl Phys 1985;57:5036–42.
[40] Nguyen H, Navid A, Pilon L. Pyroelectric energy converter using co-polymer P(VDF-TrFE) and Olsen cycle for waste heat energy harvesting. Appl Therm Eng 2010;30(14–15):2127–37.
[41] Lee FY, Navid A, Pilon L. Pyroelectric waste heat energy harvesting using heat conduction. Appl Therm Eng 2012;37:30–7.
[42] McKinley IM, Pilon L. Phase transitions and thermal expansion in pyroelectric energy conversion. Appl Phys Lett 2013;102:023906.
[43] Lee FY, R Jo H, Lynch CS, Pilon L. Pyroelectric energy conversion using PLZT ceramics and relaxor-ferroelectric phase transition. Smart Mater Struct 2013;22(2):025038.
[44] Sebald G, Pruvost S, Guyomar D. Energy harvesting based on Ericsson pyroelectric cycles in a relaxor ferroelectric ceramic. Smart Mater Struct 2008;17:1–6.
[45] Navid A, Lynch CS, Pilon L. Purified and porous poly(vinylidene fluoride-trifluoroethylene) thin films for pyroelectric infrared sensing and energy harvesting. Smart Mater Struct 2010;19:055006.
[46] Lynch CS. The effect of uniaxial stress on the electro-mechanical response of 8/65/35 PLZT. Acta Mater 1996;44:4137–9.
[47] Beer Jr FP, Johnston ER, DeWolf JT. Mechanics of materials. 4th ed. New York, NY: McGraw-Hill; 2006.
[48] Chin T, Lee FY, McKinley IM, Goljahi S, Lynch CS, Pilon L. Pyroelectric waste heat energy harvesting using 9.5/65/35 PLZT ceramics. IEEE Trans Ultrason, Ferroelectr Freq Contr 2012;59:2373–85.
[49] M Sarge S, Hemminger W, Gmelin E, Hohne GWH, Cammenga HK, Eysel W, et al. heat and heat flow rate calibration of DSC. J Therm Anal 1997;49:1125–34.
[50] Touloukian YS, Ho CY. Thermophysical properties of matter. Specific heat of metallic solids, 4. New York, NY: Plenum Press; 1972.
[51] Olsen RB, Evans D. Pyroelectric energy conversion: hysteresis loss and temperature sensitivity of a ferroelectric material. J Appl Phys 1983;54:5941–4.
[52] McKinley IM, Goljahi S, Lynch CS, Pilon L. A novel thermally biased mechanical energy conversion cycle. J Appl Phys 2013;114:224111.

Glossary

Coercive electric field: is the electric field applied to a pyroelectric material corresponding to zero electric displacement.
Curie temperature: is the temperature at which a ferroelectric material undergoes a phase transition from ferroelectric to paraelectric.
***D*–*E* loops:** are electric displacement versus electric field curves of pyroelectric materials that indicate material properties such as, large-field permittivity, coercive electric field, and remnant and saturation polarizations.
Electric displacement: is the electric charge per unit electrode area within a dielectric material. It consists of the permanent and the induced electric dipole moments in the material.
Ferroelectric materials: is a subclass of pyroelectric materials having the ability to switch the direction and magnitude of the spontaneous polarization by applying an electric field above the coercive electric field.
Morphotropic phase boundary: refers to phase transitions due to changes in composition of ferroelectric materials. It usually corresponds to the phase transition between the tetragonal and rhombohedral ferroelectric phases.
Olsen cycle: is a cycle that is performed on a pyroelectric material to utilize time-dependent temperature oscillations to convert thermal energy directly into electricity. It is sometimes known as the Ericsson cycle.
Large-field permittivity: is the slope of the ***D*–*E*** loop of a pyroelectric material at large electric field divided by the vacuum permittivity $\epsilon_0 = 8.854 \times 10^{-12}$ F/m.
Leakage current: refers to the transport of charges accumulated at the surface of a pyroelectric material through its body.
Paraelectric: refers to a state of a pyroelectric material that is in a crystal phase in which the electric dipoles are unaligned resulting in zero spontaneous polarization.
Piezoelectric materials: are dielectric materials in which the electric charge in the material and the mechanical deformation are related, i.e., an applied electric field induces a mechanical deformation and a mechanical deformation results in a change in electric displacement.
Pyroelectric materials: is a subclass of piezoelectric materials that possess a temperature-dependent spontaneous polarization.
Remnant polarization: is the polarization exhibited by a pyroelectric material under zero applied electric field.
Saturation polarization: is equal to the electric displacement in the linear fit of the ***D*–*E*** loops of a pyroelectric material at large field extrapolated to zero electric field.
Spontaneous polarization: is the average electric dipole moment per unit volume of a pyroelectric material in the absence of an electric field.
Thermal hysteresis: refers to the difference in phase transition temperatures of a pyroelectric material during heating and cooling.